Charge transfer states in phycobilisomes

Md. Wahadoszamen[1,*], Tjaart P.J. Krüger[2,*], Anjue Mane Ara[3], Rienk van Grondelle[4], and Michal Gwizdala[2,4,*,§]

[1] – Department of Physics, University of Dhaka, Dhaka 1000, Bangladesh

[2] – Department of Physics, University of Pretoria, Pretoria 0023, South Africa

[3] – Department of Physics, Jagannath University, Dhaka 1100, Bangladesh

[4] – Faculty of Science, Vrije Universiteit Amsterdam, Amsterdam 1081 HV, The Netherlands

[*] - These authors contributed equally

[§] - Corresponding author: Dr Michal Gwizdala
Department of Physics, Office 5-13, Natural Science Building 1, University of Pretoria, Private bag X20, Hatfield 0028, South Africa
E-mail: gwizdala.michal@gmail.com
Tel: +27607175821

Abstract

Phycobilisomes (PBs) absorb light and supply downstream photosynthetic processes with excitation energy in many cyanobacteria and algae. In response to a sudden increase in light intensity, excess excitation energy is photoprotectively dissipated in PBs by means of the orange carotenoid protein (OCP)-related mechanism or via a light-activated intrinsic decay channel. Recently, we have identified that both mechanisms are associated with far-red emission states. Here, we investigate the far-red states involved with the light-induced intrinsic mechanism by exploring the energy landscape and electro-optical properties of the pigments in PBs. While Stark spectroscopy showed that the far-red states in PBs exhibit a strong charge-transfer (CT) character at cryogenic temperatures, single molecule spectroscopy revealed that CT states should also be present at room temperature. Owing to the strong environmental sensitivity of CT states, the knowledge gained from this study may contribute to the design of a new generation of fluorescence markers.

Keywords: Light Harvesting/ Excitation Energy Flow Regulation/ Single Molecule Spectroscopy/ Stark Spectroscopy/ Photosynthesis

1. Introduction

Charge separation in the core of oxygenic photosynthetic reaction centers relies on the continuous supply of excitation energy from an extended network of pigments embedded in light harvesting antenna proteins [1]. By means of various molecular mechanisms regulating the flow of excitation energy, these pigment-protein antenna complexes counterbalance unexpected changes in the amount of absorbed solar energy that often occur on fast timescales, ranging from seconds to a few minutes. Upon a sudden increase in light intensity, the photoprotective qE mechanism promotes nonradiative decay of excess excitation energy in the antennae to prevent the formation of dangerous active molecular species and contributes to the non-photochemical quenching (NPQ) of chlorophyll *a* fluorescence, as its fast and reversible component [2].

In many cyanobacteria, excessive illumination triggers photoprotective mechanisms at the level of the peripheral antennae, the phycobilisomes (PBs). PB from *Synechocystis* PCC 6803 (hereafter *Synechocystis*) has a hand-shaped structure (Fig. 1A), with a central tri-cylindrical core and 6 rods fanning out from the core [3–8]. Out of up to 396 chemically identical but spectrally distinct linear tetrapyrroles covalently bound to a PB complex, 324 pigments are located in the peripheral rods. Each rod contains 2-3 phycocyanin hexamers that are characterized by room-temperature broad-band emission with the maximum near 650 nm [9–13]. In the core, 68 pigments bind to allophycocyanin with emission at ~660 nm, while the remaining pigments are red-shifted further by ~20 nm and form the so-called terminal emitters, which transfer excitation energy to the reaction centers [3,14]. The presence of multiple spectral species across a broad spectral window is an intrinsic feature of PB, not only creating a cascade for downhill energy transfer from the rods, via the core, to the terminal emitters, but also making room for several energy quenching mechanisms.

The principal photoprotective mechanism in cyanobacteria involves the orange carotenoid protein (OCP) [15], which, in its photoactivated form binds to the core of PB [16–19], creating a channel for nonradiative decay of excitations [9,10]. Another class of thermal energy dissipation mechanisms correlated with extensively red-shifted emission states, but not involving OCP, was identified in our recent exploration of the spectral properties of individual PB complexes isolated from *Synechocystis* [20]. We showed that while the fate of excitation energy in the PB complexes depends on their molecular state (e.g., a conformational state, as shown in [13,20]), the absorption of light induces switching between different states, with an increasing probability of entering a quenched state under higher light intensities within the physiological range. The role of these intrinsic quenched states (i.e., assumed in the absence of OCP) was proposed to be involved in photoprotection in two cases: 1) when the light intensity fluctuations take place on shorter timescales than the activation of OCP, and 2) in strains that do not contain OCP. In the latter, this mechanism could serve as the dominant, fast energy decay channel. It was shown that every pigmented component of PB can generate a quencher but a detailed explanation of the underlying electronic structures and excited state dynamics is still lacking. Interestingly, the large majority of far-red emission states from single, isolated PB complexes were found to be directly preceded and/or succeeded by long-living, intrinsically quenched states [21], which strongly suggests a relationship in the underlying mechanisms of those states. Again, by analogy to other photosynthetic systems, we have hypothesized that this far-red emission has a CT character. However, it needs to be attested whether the pigments in PB complexes are capable of entering states with a CT character, and whether such CT states may be involved with photoprotection in cyanobacteria.

In this study, we test the hypothesis of the existence of CT states in PBs by investigating the characteristics of the far-red spectral states as obtained from *SMS* and by applying Stark fluorescence (*SF*) spectroscopy to whole, isolated PB complexes (WT-PB) and isolated parts of PB, namely rods (ΔAB-PB) [22], cores (CK-PB) [23], as well as cores with short rods (CB-PB) [24] (Fig. 1A). As the *SF* signal evolves with the external electric field, *SF* spectroscopy is the technique of choice for revealing the CT character of photoactive species [25–28], quantify their CT character and excited-state dynamics, and for examining the electronic structures of pigments in protein matrices. It is also an effective experimental tool towards resolving multiple overlapping spectral contributions that give rise to a single broad spectral profile in conventional spectroscopy [26,29] (see also SI on *SF*). *SMS* reveals the spectral heterogeneity of photoactive complexes resulting from protein conformational disorder that is averaged out in most ensemble approaches, thus shedding light on the likelihood of accessing, e.g., states with characteristics resembling CT states [30].

2. Material and Methods

2.1. Sample preparation

The complexes WT-PB, ΔAB-PB, CK-PB and CB-PB were isolated as previously reported in Ref. [16], from WT *Synechocystis* and the mutants ΔAB [22], CK [23], and CB [24], respectively. For single molecule spectroscopy measurements the samples were prepared as described before [20]. For *SF* measurements the samples were concentrated by means of centrifugation at 3000 × *g* in Amicon Ultra-0.5 Centrifugal Filter Units (30 kDa; Merck) at room temperature until the optical density at the absorption maximum reached 100.

2.2. Single molecule spectroscopy

Measurements were performed as described in [20] using a custom setup described in [31], with sample-specific modifications described in [20]. The complexes were bound to poly-L-lysine on a microscope coverslip and excited at 594 nm, using 76 MHz pulsed light with peak intensities of 0.9 – 1.8 W/cm^2, 15 – 30 W/cm^2, and 150 W/cm^2 for WT-PB, CK-PB, and ΔAB-PB, respectively. Each complex was illuminated individually for a duration of 1 – 2 minutes and its fluorescence photons were spectrally dispersed by a diffraction grating (Optometrics LLC, HR830/800nm) and measured by a CCD camera (Spec10:100BR, Princeton Instruments) in consecutive 1-s bins. Measurements were performed at room temperature and in the presence of oxygen. Only the 30% brightest single complexes of each PB type were considered to ensure that complexes that partially degraded before the onset of the measurement were excluded from further analysis (see data screening in Ref. [20]). Note that the brightness corresponded to the intensity of an unquenched, non-shifted spectrum from the time-resolved spectral sequence of a complex.

A background spectrum was subtracted from each single-molecule spectrum. Spectra from WT-PB and CK-PB complexes exhibiting no far-red emission were fitted using a positively skewed Gaussian function for the main band and a normal Gaussian function for the vibrational wing, which typically peaked between 735 and 740 nm. Far-red emission spectra from WT-PB and CK-PB were fitted using a double skewed Gaussian function after subtracting the vibrational wing. The reported spectral parameters (width and peak position) of the far-red emission spectra reflect those of the red band in such a deconvolution. Since the peak position and width of the blue band were generally very similar to those of spectra with comparable intensity preceding and succeeding the double-band spectra, those parameters were restricted within a limited range during fitting. Spectral broadening resulting from partial quenching was fractionally divided between the two bands, based on their relative amplitudes.

To fit the spectra of ΔAB-PB, we fixed the wavelength and width of the 672 nm band, using the values reported in [13], and varied its amplitude, while keeping all variables of the blue band (near 650 nm) and far-red band free. All bands were fitted simultaneously using a positively skewed Gaussian function. To improve the fitting accuracy, the peak position and width of the blue band was again constrained as explained for the far-red spectra of WT-PB and CK-PB. No vibrational band was fitted for spectra from ΔAB-PB, because it was not possible to unambiguously discriminate between a vibrational band (related to the 650-nm emission) and far-red emission from those complexes. Data analysis was performed in MATLAB (Mathworks) and figures were prepared in Origin 9.1 (OriginLab) and Igor Pro 8 (WaveMetrics).

2.3. Stark spectroscopy

SF spectroscopy was performed on frozen PB preparations in a sucrose-containing K-phosphate buffer at pH 7.5, at 77 K in a rectangular Stark cell prepared by gluing two ITO-coated quartz slides using double-sided 100 nm thick sticky tape (Sellotape). The optical path length was determined by the thickness of the sticky tape. The *SF* experiment was carried out on a custom-built setup, similar to the one described in [27]. Briefly, the white light continuum of a Xenon lamp (Oriel) was dispersed through a monochromator (1,200 grooves/mm grating blazed at 350 nm) and the desired excitation light was selected. The excitation beam was polarized horizontally using a Glan-Taylor polarizer and directed into the sample at an angle of 45°. The sample was immersed into the liquid N_2 chamber of an Oxford cryostat (DN1704) having strain-free quartz optical windows. A low distortion sinusoidal AC voltage synthesized in the lock-in amplifier (SR850) with modulation frequency of 80 Hz was applied to the sample after desired amplification through a homebuilt high voltage generator. The polarization between the electric field and the excitation wavelength was set at the magic angle (54.7°). Both the *F* and *SF* signals were then dispersed through another monochromator (1,200 grooves/mm grating blazed at 550 nm) placed at right angle with the previous monochromator, and recorded simultaneously by a photomultiplier tube (PMT) and lock-in amplifier combination at the second harmonics of the modulation frequency. The recorded *SF* signal was then multiplied by $2\sqrt{2}$ to convert it to the equivalent DC signal and, finally, the *SF* signals were plotted as a function of wavelength to yield a *SF* spectrum.

Details about the theoretical modeling of experimentally obtained *SF* data can be found elsewhere [26,27]. Briefly, the *SF* spectrum of randomly oriented and spatially fixed photoactive chromophores in a solid matrix (having negligible inter-chromophore interaction) can be approximated as the weighted superposition of the zeroth, first and second order derivatives of the (field-free) *F* spectrum described by the following equation:

$$\frac{2\sqrt{2}\Delta F(\nu)}{F_{\max}} = (f\boldsymbol{F_{ext}})^2 \left\{ A_\chi F(\nu) + B_\chi \nu^3 \frac{d[F(\nu)/\nu^3]}{d\nu} + C_\chi \nu^3 \frac{d^2[F(\nu)/\nu^3]}{d\nu^2} \right\}, \quad (1)$$

where $F_{\max}$ is the F intensity at the maximum, $\boldsymbol{F_{ext}}$ is the magnitude of the electric field applied externally during the course of experiment, ν is the wavenumber, χ is the experimental angle between the direction of $\boldsymbol{F_{ext}}$ and the electric vector of the excitation light, and f is the local field correction factor that connects the magnitude of the internal electric field experienced by the chromophore(s) with the externally applied field via the relation $\boldsymbol{F_{int}}=f\boldsymbol{F_{ext}}$. The coefficient A_χ (denoted as the zeroth derivative contribution, ZDC) reflects the field-induced change in emission intensity arising mostly from field-induced modification of the rates of nonradiative deactivations competing with the F process [27,32,33]. The coefficients B_χ and C_χ are associated with changes in molecular polarizability ($\Delta\alpha$) and molecular dipole moment ($\Delta\mu$) between the ground and excited states connected by the optical transition, respectively.[27,32,33] At the magic angle (χ = 54.7°) the coefficients B_χ and C_χ can be expressed as [27,32]:

$$B_{54.7^\circ} = \frac{\Delta\alpha}{2\,hc} \quad (2)$$

$$C_{54.7^\circ} = \frac{(\Delta\mu)^2}{6h^2c^2}, \quad (3)$$

where h denotes the Planck constant and c the vacuum speed of light. Therefore, upon fitting the *SF* spectrum by a weighted superposition of the derivatives of the F spectrum and computing the coefficients of the first and second derivatives, one can extract the values of $\Delta\alpha$ and $\Delta\mu$ from the Eqs. (2) and (3). As the value of f is not known, the values of $\Delta\alpha$ and $\Delta\mu$ in this study are expressed in terms of f. All the *SF* spectral fitting protocols were implemented using the software routine of

Igor Pro 8 (WaveMetrics). Each of the deconvoluted bands was synthesized using a single or a linear combination of multiple skewed Gaussian functions of varying width and skewness.

3. Results

3.1. Stark Fluorescence Spectroscopy

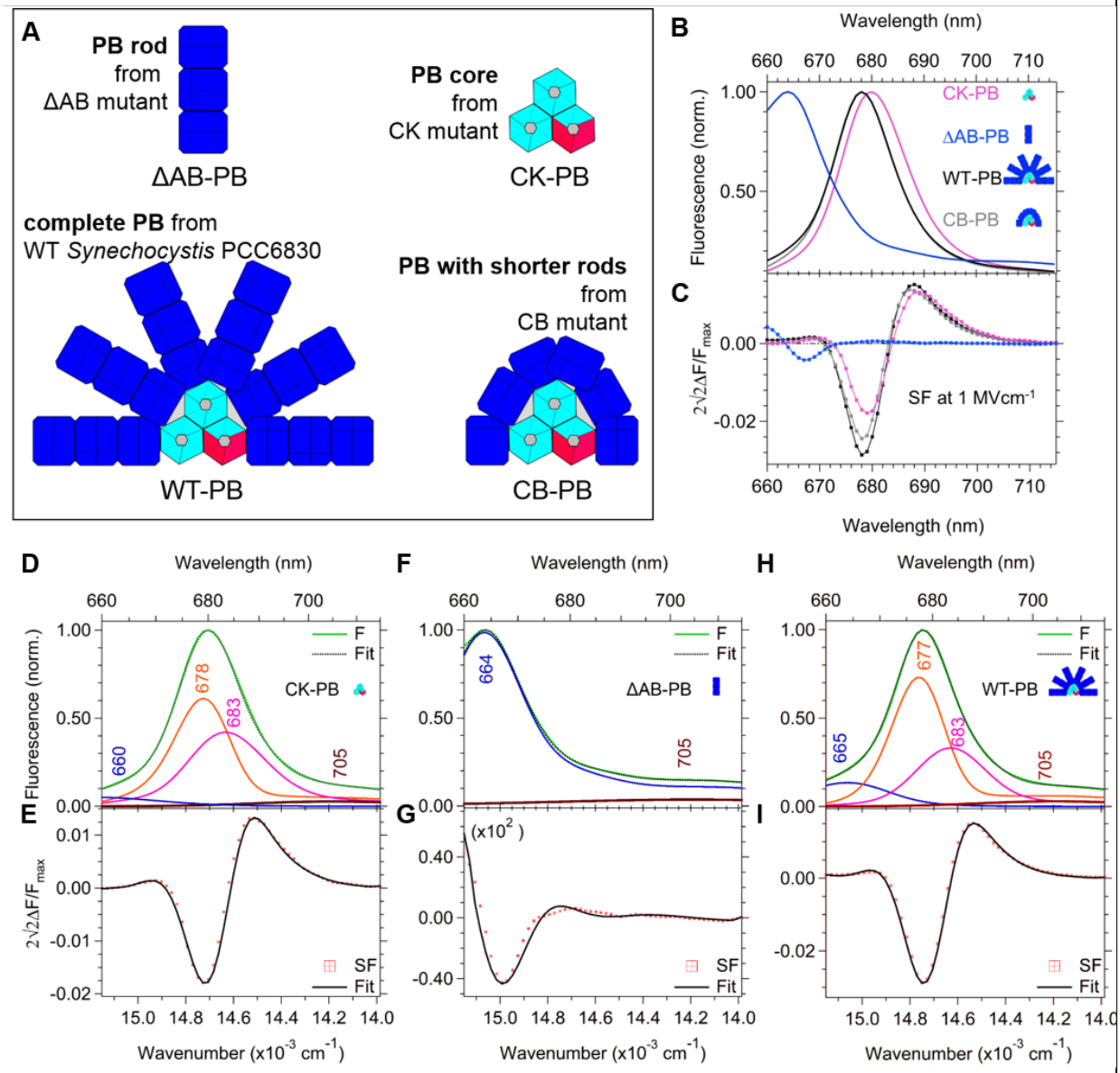

Fig. 1 (A) Complexes used in this study, isolated from wild-type *Synechocystis* PCC6803 and mutants of *Synechocystis*. Essentially, ΔAB-PB and CK-PB represent the rods (dark blue) and the core (cyan, with the ~680-nm-emitting monomers in red) of a whole WT-PB, respectively.

CB-PB has only one phycocyanin hexamer in each of its (short) rods, while WT-PB has up to three phycocyanin hexamers per rod. *F* in (B) and *SF* in (C) are spectra of WT-PB (black), CB-PB (gray), CK-PB (magenta) and ΔAB-PB (blue). The spectra were collected at 77 K upon excitation at 591 nm. Modeling of the *F* (D, F and H) and *SF* (E, G and I) spectra of CK-PB (D and E), ΔAB-PB (F and G) and WT-PB (H and I). In each case, the *F* spectrum was deconvoluted into a minimum number of constituent bands (with the peak position, λ_{max}, displayed in nm), the derivative superposition of which yielded a satisfactory fit of the corresponding *SF* spectrum. In (D, F and H**),** the far-red band (dark red) contributed about 30% of the total *F* intensity in the longer wavelength region, while the remainder was used to produce vibrational progression(s). In **(**B, D, F and H), the left insets denote the types of PB complexes used for the measurements.

Within the selected spectral window, the 77 K steady-state fluorescence (*F*) spectra in Fig. 1B are featured by a characteristic single band with a well-defined homogeneously broadened lineshape, peaking at 678 nm, 678 nm, 680 nm and 664 nm for WT-PB, CB-PB, CK-PB and ΔAB-PB, respectively, in agreement with previous reports [20]. The *SF* spectrum of each sample is characterized by an intense negative band (whose peak is located in the vicinity of the corresponding *F* peak) and asymmetric positive wings on both sides (Fig. 1C), thereby yielding a typical derivative-like Stark lineshape (see SI) [34].

To uncover the underlying electronic structures (i.e., the electro-optical parameters) and excited-state dynamics of the contributing spectral species, the *SF* spectra were analyzed by employing the conventional Liptay formalism (see also SI). According to this formalism, a linear combination of the zeroth, first and second derivatives of the *F* spectrum [35,36] is used to fit the *SF* spectrum in a certain spectral window when the associated *F* signals originate from a single

type of non-interacting pigments. For complexes containing spectrally different pigments, each pigment type has distinct electro-optical parameters, giving rise to a distinct *SF* signal, and a sum of independent linear equations should be used to fit the *SF* spectrum. Although PB from *Synechocystis* contains only one type of pigment, the phycocyanobilin, the spectral properties of the pigments in the cores and the rods are distinct and, therefore, a sum of independent linear equations was used.

We approached the *SF* spectra of PBs in a systematic way by firstly analyzing the spectra of CK-PB and ΔAB-PB, representing the cores and the rods, respectively, of the whole PB complex. The spectral parameters obtained from this analysis were then used to fit the more congested spectra of the whole PB antenna. The *F* emission from CK-PB originates mainly from a state equilibrated over pigments emitting near 660 nm and the terminal emitter pigments emitting around 680 nm [12]. As a result, the simplest fitting model of the *F* spectrum gives a single, intense 680-nm band and a weak 660-nm band (Fig. S2A). However, for such deconvolution, the best fit of the *SF* spectrum (Fig. S2B) deviated strongly from the experimental data, in particular above 680 nm, indicating that the intense 680-nm emission of the *F* spectrum is a superposition of more than one spectral species, each having a distinct set of electro-optical parameters. In Figs S2C and D, the *F* and *SF* spectra were fitted using a model where the 680-nm band was deconvoluted into two independent bands peaking at 678 and 683 nm, respectively. In this case, it was assumed that the *F* intensity in the longer wavelength region (above 690 nm) constitutes vibrational progression and was hence distributed proportionately to the red tails of the two bands. Although this model reproduces the main *SF* spectral features (Fig. S2D), it still noticeably deviates from the *SF* spectra above 690 nm, suggesting that the *F* intensity above 690 nm is not purely due to vibrational progression of the two bands. Instead, it must have a contribution from another distinct spectral

band. Figs 1D and E show that a satisfactory fit of the *SF* spectrum can be obtained by adding a broad and strongly red-shifted emission band. Owing to the lack of quantitative information about the amplitude of the far-red emission band as compared to the vibrational tails, we estimated a 30% contribution of the far-red band to the total *F* intensity above 690 nm. Therefore, the *F* spectrum of CK-PB was ultimately deconvoluted into four constituent bands peaking at 660 nm, 678 nm, 683 nm, and 705 nm, respectively. Table 1 summarizes the molecular parameters estimated from the analysis.

A similar approach was followed to fit the *SF* spectra of ΔAB-PB, representing the PBs' rods. When considering the *F* spectrum to consist of a single band with a vibrational tail (Fig. S2A) the derivative superposition of this spectrum led to a non-negligible disagreement with the *SF* data above 680 nm (Fig. S2B). Addition of a separate, independent band above 700 nm considerably improved the fit of the *SF* spectrum in the long-wavelength region (Fig. 1G). The *F* spectrum was deconvoluted into two bands peaking at 664 nm and 705 nm (Fig. 1F), and the *SF* spectrum of ΔAB-PB was again obtained by the weighted superposition of the derivatives of the deconvoluted bands. Similar to CK-PB, the 705 nm band was estimated to account for 30% of the *F* intensity at longer wavelengths. The molecular parameters estimated from the analysis are included in Table 1.

Figs 1E and G indicate that introduction of an independent, broad, significantly red-shifted band (peaking beyond 700 nm) was a fundamental requirement for obtaining satisfactory fits of the *SF* spectra of CK-PB and ΔAB-PB. For both samples, this far-red band was associated with a considerable magnitude of the dipole moment, $\Delta\mu$, signifying a state with a prominent CT character (see Table 1).

Similar deconvolution protocols were applied to analyze the *SF* spectra of CB-PB and WT-PB. Since CK-PB is the complete core of PB and ΔAB-PB can be seen as representing the rods of the PB antenna [22,37], one can consider the *F* spectra of CB-PB and WT-PB to be composed of the combined *F* bands of CK-PB and ΔAB-PB. To simplify the model, we represented analogous bands from CK-PB and ΔAB-PB by a single band; for example, the 660-nm band of CK-PB and the 664-nm band of ΔAB-PB were not considered as distinct bands in the models for CB-PB and WT-PB. Like for CK-PB and ΔAB-PB, the *SF* spectrum of CB-PB and WT-PB could not be adequately fitted when only including the vibrational progression associated with the 677 nm and 683 nm bands but excluding the far-red band (Fig. S3). Inclusion of a 705 nm band contributing to about 30% of the *F* intensity above 690 nm significantly improved the fits of the *SF* spectra of WT-PB (Figs 3H and I) and CB-PB (Fig. S4), both of which consisted of a weighted superposition of the derivatives of four bands, peaking at 665 nm, 677 nm, 683 nm and 705 nm, respectively. In essence, the 677 nm and 683 nm bands replicate the spectral constituents of CK-PB at similar wavelengths, while the other two bands originate from both the core and the rods. Once again, the far-red states have large $\Delta\mu$ magnitudes (see Table 1).

SF spectroscopy, as a method sensitive to CT states, unambiguously revealed the contribution of these states to the spectroscopic signal of PBs at 77 K. The ability of electronic excitations in PBs to access CT states is unexpected. It is striking that the far-red spectral states accessed occasionally and reversibly by individual, whole PB complexes at room temperature, revealed in our recent *SMS* studies [20,21], have similar peak positions as the far-red bands identified with *SF* in this work. To determine a possible relationship between the far-red states identified via *SF* spectroscopy and *SMS*, we investigated whether the far-red states of individually measured PBs show characteristics resembling those of CT states.

3.2. Single Molecule Spectroscopy

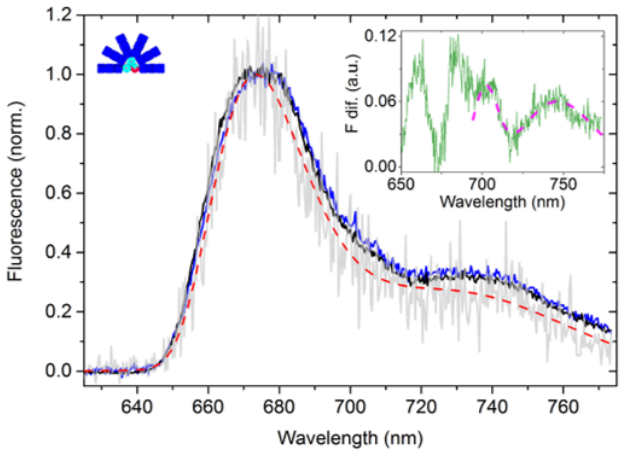

Fig. 2 Room-temperature bulk spectrum of WT-PB (black) compared with the average of 4000 randomly selected single molecule spectra (blue) and a representative 10-s averaged single molecule spectrum of a WT-PB complex in an unquenched state (gray). For bulk, a 12 nM solution of freely diffusing complexes was excited; each single molecule spectrum originated from a different substrate-bound WT-PB complex. Spectra were measured consecutively on the same optical setup. A 4-min averaged background spectrum was subtracted from the black and blue spectra and a 10-s averaged background spectrum was subtracted from the gray spectrum. The right inset shows the difference between the bulk spectrum (black) and the double skewed Gaussian fit (red dashed line) of the single-molecule spectrum. The red part of the difference spectrum was fitted with two Gaussians (magenta dashed line) with peak positions at 702 and 746 nm. The left inset denotes the type of sample used in the measurements (WT-PB).

Fig. 2 shows that the addition of a large number of random single-molecule PB fluorescence spectra converges to that of the ensemble, indicating that the single-molecule environment had a negligible effect on the complexes. A typical spectrum of an individual complex in a bright, unquenched state resembled the bulk spectrum but showed a clear deviation in three regions. First, the main band is narrower, indicating that static disorder contributes to broadening of the bulk spectrum (*vide infra*, Fig. 3E). Furthermore, the red wing has lower intensity, giving rise to what appears as two positive bands in the difference spectrum between the bulk and single molecule spectra (Fig. 2 inset), peaking near 700 nm and 750 nm. The nature of these two red-shifted bands was investigated further by examining the spectral characteristics of individual WT-PB, CK-PB, and ΔAB-PB complexes using *SMS*.

The ability of PB to reversibly switch between unquenched, quenched and red-shifted emission states, as revealed in previous studies [20,21], is portrayed by switches between at least three dominant, quasistable substates of its free energy conformational landscape (Fig. 3A). Fig. 3B shows a representative spectral sequence from a single WT-PB complex that switched reversibly into a far-red emission state, visible as an enhancement near 700 nm on top of the broad vibrational wing, after being in a strongly quenched state for several seconds. While the far-red emission was always observed as a red-shifted band in addition to the main, ensemble-like band (hereafter the “blue band”), the spectra before and after the far-red emission reflect those of the ensemble-averaged *F* spectra of PBs (see also Fig. 2). A recent study showed that the intensity ratio of the blue and far-red spectral bands in this characteristic double-band spectral profile can be explained by a single pigment in the core acting as the site of far-red emission [21].

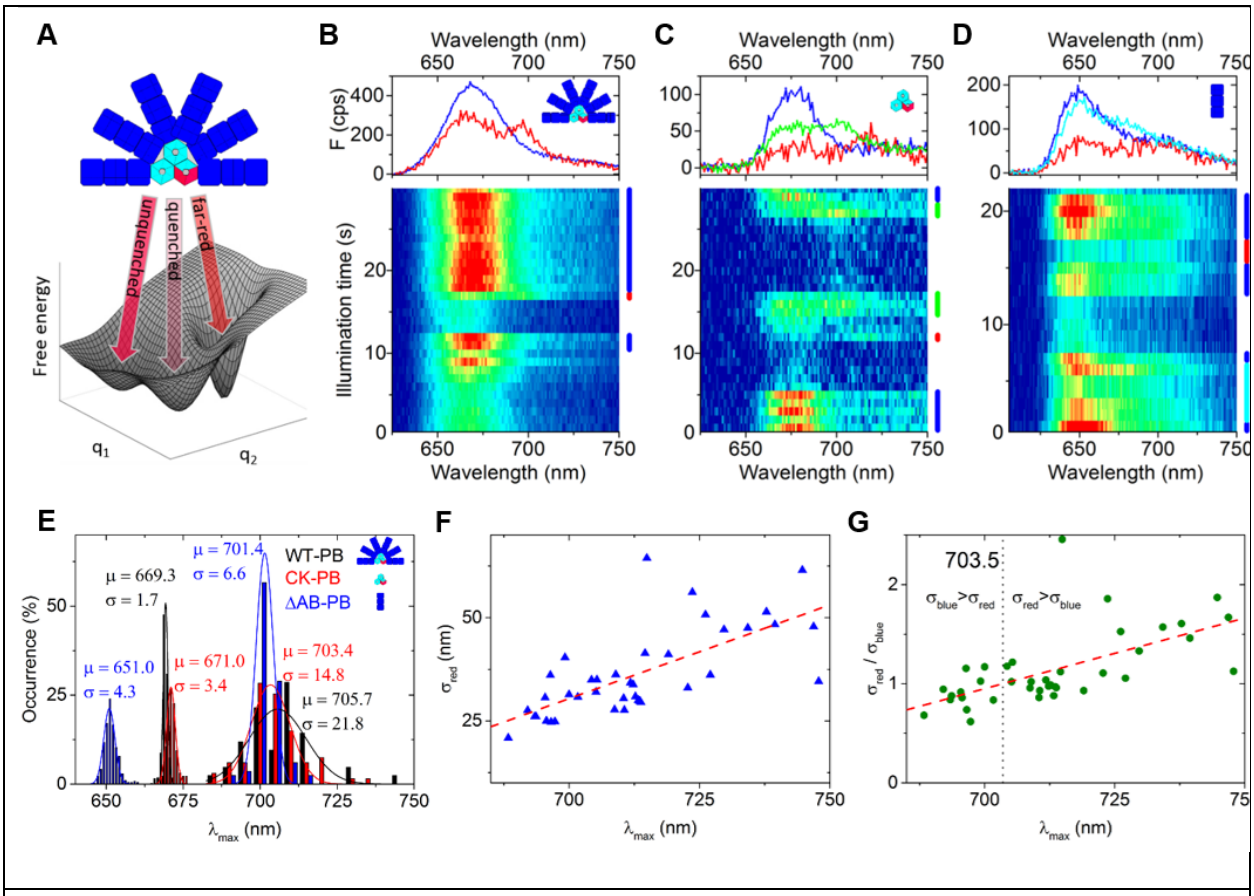

Fig. 3 (A) By means of reversible switches between different conformational states, illuminated PBs assume different minima in their free energy landscape, portrayed here as a function of two nuclear coordinates, which are signified by three major spectroscopic states: unquenched, quenched and far-red. Room-temperature *F* spectral sequence of a single WT-PB (B), CK-PB (C), and ΔAB-PB (D). Spectra on top are averages of the spectra in the map corresponding to the times indicated by the color-coded bars on the right of each spectral trace. In (E), peak distributions of far-red emission bands (λ_{max} > 680 nm, 5-nm bins) compared to peak distributions of ensemble-like spectra (i.e., devoid of far-red emission bands) (λ_{max} < 680 nm, 1-nm bins). Each distribution is scaled separately. The total number of quasi-stable, reversible, far-red spectra are 46, 67, and 83 from 42 WT-PB, 42 CK-PB and 44 ΔAB-PB complexes, respectively, selected from a few hundred individually measured complexes (the selection

allows to focus on intact, biologically relevant complexes only). Fitting details are described in the Experimental section and an example is shown in Fig. S5. For spectra devoid of far-red emission bands, only unquenched states were considered to enhance the fitting accuracy. Since λ_{max} of ΔAB-PB's 672-nm band was fixed it is not shown. Gaussian fits of the peak distributions are displayed (black curves), along with the mean value (μ, in nm) and the full-width at half-maximum (σ, in nm) of each fit. In **(**F), relationship between the full-width at half-maximum and peak position of the far-red emission bands from WT-PB. In **(**G), ratio of the full-width at half-maximum of the far-red and blue bands of spectra with far-red emission as a function of the far-red spectral peak. The dashed lines in (F and G) denote linear regressions. Dotted vertical line in (G) is at 703.5 nm. In (B, C, D and E), the right insets denote the types of PB complexes used for the measurements.

Far-red spectra with similar characteristics were observed from single PB complexes isolated from the CK and ΔAB mutants. Representative spectral sequences, showing reversible switches into far-red emission states are shown in Figs 3C and D, respectively. The example in Fig. 3C shows switches between different far-red states in CK-PB (red and green spectra), a behavior occasionally also observed for single WT-PB complexes. ΔAB-PB displayed the greatest dynamics, in particular with respect to the relative amplitude around 670 nm (Fig. 3D, cyan spectrum), suggesting the presence of a distinct emission band near 670 nm. In our recent study on this complex [13] we showed that the *F* spectra of all ΔAB-PB complexes have a distinct ("red") band peaking near 672 nm. Inspection of the spectra from different individual complexes indicated that the peak position, λ_{max}, of the ~672-nm band was mostly constant, while that of the >690-nm, "far-red" emission varied across a broad range. However, the far-red emission states, clearly

present beyond 690 nm (Fig. 3D, red spectrum) were not investigated in the previous study [13] and form the focus of this work.

For all investigated types of PBs, λ_{max} of the far-red states was stable for times ranging between sub-seconds and tens of seconds before the emission generally switched back to the original ensemble-like spectral shape [21]. The timescale of the spectral diffusion suggests that the spectral switches are governed by protein conformational (static) disorder (Fig. 3A), similarly to the other types of spectral dynamics investigated previously [13,20].

While most far-red emission states were characterized by a quasistable λ_{max} for a given complex, there was a large complex-to-complex variation. This was investigated quantitatively by selecting all WT-PB, CK-PB and ΔAB-PB complexes that exhibited far-red emission and comparing the λ_{max} distribution of their far-red bands with that of the ensemble-like blue bands (Fig. 3E). For WT-PB and CK-PB, the far-red λ_{max} distributions extend from below 690 nm to ~740 nm, while ΔAB-PB featured a slightly narrower distribution. The far-red peak distributions for all three samples are considerably broader than those of the ensemble-like blue bands (Fig. 3E). In all three cases the maxima of the distributions were just beyond 700 nm (~701-706 nm).

Fig. 3F shows that the width of the far-red bands displays a linear correlation with the peak position. Also, the relative width of the far-red band with respect to the accompanying blue band increases linearly with the peak wavelength and becomes broader than the latter, on average, above 703.5 nm (Fig. 3G). Since the blue band is comprised of multiple spectral components (Fig. 2 and Refs. [12,20]), the far-red emission features an excessively broad spectrum.

Table 1: Spectral fitting and estimated electro-optic parameters (with standard deviations). Peak amplitude is compared with unity. The abbreviations denote: FWHM – full-width at half-maximum, ZDC – zeroth derivative contribution, $\Delta\alpha$ – change in the molecular polarizability, and $\Delta\mu$ – change in the dipole moment.

	Band (nm)	**Peak Intensity (a.u.)**	**FWHM (nm)**	**ZDC (%) (at 1 MVcm^{-1})**	**$\Delta\alpha$ (Å^3/*f*^{2})**	**$\Delta\mu$ (D/*f*)**
CK-PB	660	0.05	22	0.50 ± 0.01	-72 ± 3	0.00
	679	0.61	14	-5.3 ± 0.2	-47 ± 1	1.9 ± 0.2
	683	0.42	20	5.5 ± 0.2	-54 ± 2	1.5 ± 0.2
	705	0.03	44	9.0 ± 0.2	-716 ± 28	9.2 ± 0.6
ΔAB-PB	664	0.98	14	0.4 ± 0.01	-64 ± 3	1.9 ± 0.3
	705	0.04	40	0.4 ± 0.01	-36 ± 3	5.7 ± 0.6
WT-PB	664	0.13	22	-1.0 ± 0.1	-143 ± 3	2.1 ± 0.2
	678	0.73	13	-5.1 ± 0.2	-115 ± 1	1.9 ± 0.2
	683	0.33	18	7.5 ± 0.2	-54 ± 2	1.5 ± 0.2
	705	0.03	44	10.0 ± 0.2	-716 ± 28	9.2 ± 0.6
CB-PB	664	0.11	22	-2.0 ± 0.1	-143 ± 3	2.1 ± 0.2
	678	0.73	13	-4.3 ± 0.2	-107 ± 1	1.9 ± 0.2
	683	0.33	18	6.8 ± 0.2	-54 ± 2	1.5 ± 0.2
	705	0.03	44	8.5 ± 0.2	-716 ± 28	9.2 ± 0.6

4. Discussion

For numerous other photosynthetic pigment-binding complexes displaying similar far-red emission, theoretical studies have indicated that these characteristics can only be explained adequately when considering CT states mixed with singlet excited states [38]. This mixing generates a CT state with a weak emissive character as well as one or more excited states with some CT character [39–41], the latter of which are sufficiently low in energy to be populated. Furthermore, CT states are known to couple more strongly to fast environmental vibrations (phonons) than the excited states of the same pigments [42–44], giving rise to significant homogeneous line broadening [40,42,45] and increased optical reorganization energy, leading to an enhanced Stokes shift [39–42,46]. The far-red states of individual PBs clearly show evidence of large Stokes shifts (Fig. 3E) and significant spectral broadening (Fig. 3G) as well as a direct relationship between the two (Fig. 3F), suggesting a common underlying mechanism (i.e., strong coupling to phonons). Furthermore, the mixing strength determines the polarity of the hybrid state [39,40], which is very sensitive to the charged protein microenvironment of the embedded pigments. The spectroscopic properties of the hybrid state, especially its energy, are therefore very sensitive to the mixing strength and consequently also to dynamic and static disorder [44,47]. An enhanced sensitivity to dynamic disorder explains well the broad spectral widths of the far-red states (Fig. 3G), while the effect of static disorder explains the broad far-red peak distributions in Fig. 3E and the occasional shifts between different quasistable far-red states (Fig. 3C).

Upon formation of the hybrid state, the emission intensity is reduced due to some borrowing of intensity by the dark CT state from the excited state [39]. The resulting enhancement in nonradiative decay corroborates the reduced brightness of the far-red states of WT-PB analyzed in a recent study [21], showing that these states are on average ~35% quenched compared to

spectrally non-shifted emission states and have fluorescence lifetimes that are similarly shortened. Finally, a theoretical study on the Photosystem II reaction center showed that a shift of the CT state to lower energies resulted in an enhanced amplitude of the red wing of the fluorescence spectrum from ~700 nm to beyond 760 nm [47]. This suggests that far-red emission (near 700 nm) resulting from CT-exciton mixing in that complex is accompanied by an enhanced vibrational wing of the fluorescence spectrum (between ~730 and ~760 nm), which may also explain the enhanced vibrational wing of PB in Fig. 2 due to the presence of a similar mixed state.

From our *SMS* measurements we have thus identified various properties of the far-red emission states of single PB complexes that are generally characteristic of emission states with a CT character, viz. 1) a large Stokes shift, 2) spectral broadening, 3) strong spectral heterogeneity, 4) partial quenching, and 5) an enhanced vibrational wing.

A key finding in this study is that for all investigated samples the *SF* measurements showed the existence of a spectral band peaking above 700-nm and that the standard Liptay formalism yielded a large magnitude of $\Delta\mu$ for this spectral species, indicating a strong CT character. These two properties are corroborated by the *SMS* results: far-red spectral bands were observed for all samples and show behavior reminiscent of a state with CT character. We conclude that the two experimental approaches revealed the same far-red states. The >700-nm spectral band observed from the *SF* study is then a superposition of a broad distribution of bands observed from the *SMS* study, with peak positions ranging between ~690 nm and ~740 nm and with emission between 700 nm and 710 nm occurring most abundantly. The broad spectral distribution is explained by the sensitivity of CT states to the local protein environment and is consistent with the excessively broad bandwidth of the far-red state in the *SF* spectra (see also SI on *SF*). Furthermore, the necessity of including >700-nm bands in the *SF* analysis, justified also by the comparison of

unquenched single-molecule spectra with the ensemble (Fig. 2), and their large associated $\Delta\mu$ values suggest that a sizable subpopulation of complexes exhibits a strong CT state at any time during illumination, or that all complexes possess a permanent CT state that may mix with the excited singlet state dependent on the realization of the protein disorder. In other words, far-red emission contributes to the emission of an ensemble of isolated PB complexes as the result of some fraction of complexes always being in a far-red state when illuminated (Fig. 2).

To our knowledge, besides CT states, no other previously characterized molecular mechanism taking place at the level of PBs can explain the reversible entering of PB pigments into partly-quenched far-red emissive states. Firstly, radical cations, previously proposed to be responsible for energy quenching in allophycocyanin trimers and monomers [48,49] absorb light but do not emit and, therefore, cannot explain the far-red emission. Since the far-red states are correlated with the quenched states in PBs [21], radical cations are also, most likely, not responsible for light-induced energy quenching in PBs or their separate components. Moreover, it is important to point out that the formation of radical cations in allophycocyanin was demonstrated upon irradiation with UV radiation at 248 nm [50], while the far-red states discussed here and PBs' quenched states in general were shown to be induced by visible light [20,21,48,49,51]. Secondly, being only partly quenched, the far-red states in PBs remain emissive, distinguishing themselves from the molecular states assumed by the tetrapyrroles in phytochromes and other, phytochrome-like proteins. In fact, in contrast to phytochromes, most phycobiliproteins [52], and all in this study, are not photoactive. The pigment binding sites in PBs are tightly packed, leaving no space for large configurational changes of pigments such as light-induced torsions of pyrrole rings involved in the photoconversion of phytochromes [53]. Thirdly, a reversible change in the protonation state of the PB pigments also fails to explain the far-red states in PBs. Tetrapyrroles in PBs and, e.g., in the

phycobiliproteins from cryptophyte algae, were shown to be fully protonated [54–56]. Light-induced deprotonation of one of the pigments in PBs from *Synechocystis* is expected to induce a blue shift of emission [57]. Finally, since our *SMS* measurements are performed *in vitro*, on isolated PBs complexes, all enzymatic modifications of PBs taking place in the cells and impacting the spectroscopic properties of bound tetrapyrrole pigments [58,59] can be ruled out as a possible mechanism behind the red states. On the other hand, a time-resolved study on phycocyanobilins isolated from PBs pointed at the presence of a light-induced component, signified by a red-shifted absorption spectrum ("species C"), contributing to the room-temperature ensemble spectrum of these pigments [60]. Interestingly, the relative contribution of species C to the absorption spectrum depended on the solvent [60] and the larger contribution in methanol than in n-octanol could be explained by the fact that CT states are known to be more stable in more polar environments.

This work does not address the long-standing discussion of whether pigments in the core of PBs are within the strong or weak dipole-dipole interaction regime [61]. Instead, we focus here on identifying the origins of the light-induced CT state in PBs. Due to the large distances between neighboring pigments in PB complexes, we rule out the possibility of formation of an interpigment CT state, which is in contrast to chlorophyll-containing protein complexes where the CT character was ascribed to excitonically coupled pigments [31,62]. This assumption is in agreement with the recent results and model by Wang and Moerner [51] and takes into consideration the fact that the absorption spectrum of the ApcE dimer, with the pigments unequivocally within the FRET regime, is similar in shape to the absorption spectrum of the allophycocyanin trimers [63]. Therefore, in PB complexes, the CT state is either an intramolecular charge transfer state formed within one of the pigments or is the result of interaction between a pigment and one or more closely separated amino acid residues. In either case, strong mixing of the singlet excited state with a CT state is

necessary for the former to gain CT character. The CT states in PBs are light induced and likely stabilized or governed by pigment-protein interactions.

Our results show that far-red states occur both at room temperature and at 77 K and cannot be fully rationalized by vibrational progression or mechanisms other than CT states. The results also strongly suggest that *SMS* and *SF* spectroscopy revealed the same far-red states and that the states resolved from the *SMS* studies do not result from highly improbable or unphysiological conformations (Fig. 2). Moreover, the position of the far-red fluorescence band with strong CT character revealed by *SF* spectroscopy matches that of the far-red single molecule spectral bands (Fig. 3E, see also Fig. 2, inset). In general, the presence of CT-related far-red emission at 77 K suggests that similar emission is likely to occur also at higher temperatures, albeit with a smaller relative amplitude due to thermal equilibrium [42].

Moreover, mixing of a CT state into one or more excited states of the pigment may lead to large negative $\Delta\alpha$ values [26,43]. For all types of PB in this study, the values of $\Delta\alpha$ and $\Delta\mu$ are comparable for the analogous bands (see Table 1), which is expected for emission signatures of the same species. Similar molecular parameters indicate the same or similar electronic structures. However, as the microenvironment of related pigments may be somewhat different for the different types of PB, small variations in the band intensity of analogous bands and ZDC values are expected, because the ZDC coefficients are very susceptible to the local protein environment of the pigments.

In general, the presence of multiple distinct spectral states comprising the broad *F* spectra can be explained by a Boltzmann energy distribution across the various subunits of PBs combined with the functional plasticity of the (chemically identical) pigments in the PB complex. Interestingly, the 677/678-nm and 683-nm bands are associated with similar values for $\Delta\alpha$ and $\Delta\mu$,

both in sign and amplitude (when the parameters were free during analysis), but the values for ZDC are strikingly different, both in sign and magnitude (see Table 1). The similarity of the values for $\Delta\alpha$ and $\Delta\mu$ suggests that the pigment species related to the 677/678-nm and 683 nm emission bands have similar electro-optical or molecular parameters, which agrees with previous studies showing that these two bands correspond to different types of terminal emitting pigment-protein complexes, namely ApcE and ApcD [17,64]. However, the opposite signs of ZDC indicate that the two spectral species have different excited state dynamics, resulting most likely from encapsulation of the emissive species by different local protein environments and/or a different configuration of the pigment in the binding site, the latter being shown in a recent report [65]. Since we are dealing with chemically identical pigments, the two spectral bands should also be associated with different types of nonradiative deactivation channels. The rates of nonradiative processes may experience very different modulation by an externally applied electric field, thus providing a reason for the different signs and amplitudes of ZDC for the two bands. Specifically, the negative and positive signs of ZDC indicate that the nonradiative rates of the 677/678-nm and 683-nm emission states are enhanced and reduced by the electric field, respectively.

We also conclude that the room-temperature ~672-nm, red (in contrast to far-red) emission band of phycocyanin rods does not involve a strong CT character as signified by a relatively small value of $\Delta\mu$ of the 664-nm band at 77 K. In contrast to typical far-red states with a CT character, the ~672-nm states of phycocyanin are not quenched, supporting the hypothesis that they are not involved in energy dissipation [13].

A unique combination of *SMS* and *SF* spectroscopy has allowed us to identify a number of new spectroscopic states in PB pigment-protein complexes and to obtain a detailed description of their electro-optical properties. This information is usually hidden beneath the broad bands of

steady-state room temperature and 77 K spectra. Our *SMS* study showed that, while the far-red vibrational wing is a permanent feature of the *F* spectrum of a PB complex, enhanced far-red emission is a dynamic property of the complex, varying in amplitude, energy, instant of occurrence, and duration. Switching into and out of such a far-red state is likely governed by conformational changes [13,20,66] and is clearly light-induced [20,21]. Furthermore, the rods and the cores of PB complexes can switch into these states independently.

The far-red states occur occasionally but their physiological importance should be viewed in connection with the associated strongly quenched states [21]. Two recent *SMS* studies [21,67] have shown an explicit relationship between the far-red states and thermal energy dissipation states in PB. While these studies do not allow us to conclude whether a common mechanism underlies the intrinsic light-induced and OCP-induced quenched states, they show that CT states play a crucial role in the regulation of excitation energy flow in the photosynthetic apparatus of cyanobacteria. Since the connection between far-red and quenched states points at a common underlying molecular mechanism, it is very likely that this energy dissipation mechanism involves a CT state [21]. Identification and characterization of the role of CT states in the regulation of light harvesting antenna complexes deepens our understanding of the early stages of photosynthesis at the fundamental, molecular level, constituting a basis for the development of novel bio-inspired solar technologies that are capable to adapt to constantly changing light conditions and to make the best use of available energy.

Outside the research fields focused on photosynthesis and phytochrome-type photoreceptors, proteins that bind linear tetrapyrroles have recently attracted attention as promising fluorescence markers for *in vivo* and bio-medical purposes [68–71]. This interest can be explained by: 1) the synthesis of linear tetrapyrroles requiring only a few enzymatic reactions

(usually between 1 and 3), starting from the heme, a common substrate found in all organisms, and, 2) these pigments being embedded in protein matrices can achieve extremely high fluorescence brightness. As shown in previous studies, as well as in this work, the protein matrix plays a critical role in the tuning of the optical properties of these pigments, opening a possibility for protein engineering of designs whose emission properties are optimized for specific applications like in bio-medical technologies. The presence of CT states in those pigments can make these possibilities even more exciting by leading to a new generation of fluorescence markers, which, thanks to the sensitivity of CT states, would be capable of accurately reporting changes in the chemical environment of the fluorescence marker and the target of interest.

Author's contributions

MdW, TPJK, RvG and MG, designed the research and interpreted the results. MG isolated the samples and performed the *SMS* measurements. MdW and MG performed *SF* measurements. TPJK analyzed the *SMS* data. MdW and AMA analyzed the *SF* data. MdW, TPJK and MG wrote the manuscript.

The authors declare no competing financial interests.

Acknowledgments

We would like to acknowledge Dr Diana Kirilovsky for kindly letting us use her laboratory to obtain the samples used in this study. We thank Dr Ghada Ajlani for the kind gift of the mutant strains of *Synechocystis*, from which the samples were isolated. The work of all authors was supported from an advanced investigator grant (267333, PHOTPROT) from the European Research Council and the TOP grant (700.58.305) from the Foundation of Chemical Sciences part of NWO, both awarded to RvG. TPJK was supported by the National Equipment Programme of the National Research Foundation (NRF) (grant N00500, project 87990), NR*F* Thuthuka programme (grant N00726, project 94107) and the Photonics Initiative of South Africa. RvG gratefully acknowledges his 'Academy Professor' grant from the Royal Netherlands Academy of Arts and Sciences (KNAW). MG is thankful for his EMBO long term fellowship, Claude Leon Foundation Postdoctoral Fellowship and Senior Postdoctoral fellowship at the University of Pretoria.

References

[1] R. van Grondelle, J.P. Dekker, T. Gillbro, V. Sundstrom, Energy transfer and trapping in photosynthesis, Biochim. Biochim. Biophys. Acta Bioenerg. 1187 (1994) 1–65. https://doi.org/10.1016/0005-2728(94)90166-X

[2] B. Demmig-Adams, G. Garab, W. Adams III, Govindjee, eds., Non-Photochemical Quenching and Energy Dissipation in Plants, Algae and Cyanobacteria, Springer Netherlands, Dordrecht, 2014. http://link.springer.com/10.1007/978-94-017-9032-1 (accessed June 22, 2015).

[3] A.N. Glazer, Phycobilisome: a macromolecular complex optimized for light energy transfer, Biochim. Biophys. Acta. 768 (1984) 29–51. https://doi.org/10.1016/0304-4173(84)90006-5

[4] A. Arteni, G. Ajlani, E. Boekema, Structural organisation of phycobilisomes from Synechocystis sp strain PCC6803 and their interaction with the membrane, Biochim. Biophys. Acta Bioenerg. 1787 (2009) 272–279. https://doi.org/10.1016/j.bbabio.2009.01.009.

[5] H. Liu, H. Zhang, D.M. Niedzwiedzki, M. Prado, G. He, M.L. Gross, R.E. Blankenship, Phycobilisomes Supply Excitations to Both Photosystems in a Megacomplex in Cyanobacteria, Science. 342 (2013) 1104–1107. https://doi.org/10.1126/science.1242321.

[6] N. Adir, Elucidation of the molecular structures of components of the phycobilisome: reconstructing a giant, Photosynth. Res. 85 (2005) 15–32. https://doi.org/10.1007/s11120-004-2143-y.

[7] M. Watanabe, M. Ikeuchi, Phycobilisome: architecture of a light-harvesting supercomplex, Photosynth. Res. 116 (2013) 265–276. https://doi.org/10.1007/s11120-013-9905-3.

[8] R. MacColl, Cyanobacterial phycobilisomes, J. Struct. Biol. 124 (1998) 311–334.

[9] L. Tian, I.H.M. van Stokkum, R.B.M. Koehorst, A. Jongerius, D. Kirilovsky, H. van Amerongen, Site, rate, and mechanism of photoprotective quenching in cyanobacteria, J. Am. Chem. Soc. 133 (2011) 18304–18311. https://doi.org/10.1021/ja206414m.

[10] L. Tian, M. Gwizdala, I.H.M. van Stokkum, R.B.M. Koehorst, D. Kirilovsky, H. van Amerongen, Picosecond Kinetics of Light Harvesting and Photoprotective Quenching in Wild-Type and Mutant Phycobilisomes Isolated from the Cyanobacterium Synechocystis PCC 6803, Biophys. J. 102 (2012) 1692–1700. https://doi.org/10.1016/j.bpj.2012.03.008.

[11] A.R. Holzwarth, Structure-function relationships and energy transfer in phycobiliprotein antennae, Physiol. Plant. 83 (1991) 518–528. https://doi.org/10.1111/j.1399-3054.1991.tb00129.x.

[12] I.H.M. van Stokkum, M. Gwizdala, L. Tian, J.J. Snellenburg, R. van Grondelle, H. van Amerongen, R. Berera, A functional compartmental model of the Synechocystis PCC 6803 phycobilisome, Photosynth. Res. (2017) 1–16. https://doi.org/10.1007/s11120-017-0424-5.

[13] M. Gwizdala, T.P.J. Krüger, M. Wahadoszamen, J.M. Gruber, R. van Grondelle, Phycocyanin: One Complex, Two States, Two Functions, J. Phys. Chem. Lett. 9 (2018) 1365–1371. https://doi.org/10.1021/acs.jpclett.8b00621.

[14] D.J. Lundell, A.N. Glazer, Molecular architecture of a light-harvesting antenna. Structure of the 18 S core-rod subassembly of the Synechococcus 6301 phycobilisome., J. Biol. Chem. 258 (1983) 894–901.

[15] A. Wilson, G. Ajlani, J. Verbavatz, I. Vass, C. Kerfeld, D. Kirilovsky, A soluble carotenoid protein involved in phycobilisome-related energy dissipation in cyanobacteria, Plant Cell. 18 (2006) 992–1007. https://doi.org/10.1105/tpc.105.040121.

[16] M. Gwizdala, A. Wilson, D. Kirilovsky, In Vitro Reconstitution of the Cyanobacterial Photoprotective Mechanism Mediated by the Orange Carotenoid Protein in Synechocystis PCC 6803, Plant Cell. 23 (2011) 2631–2643.
[17] D. Jallet, M. Gwizdala, D. Kirilovsky, ApcD, ApcF and ApcE are not required for the Orange Carotenoid Protein related phycobilisome fluorescence quenching in the cyanobacterium Synechocystis PCC 6803, Biochim. Biophys. Acta Bioenerg. 1817 (2012) 1418–1427. https://doi.org/10.1016/j.bbabio.2011.11.020.
[18] A. Wilson, C. Punginelli, A. Gall, C. Bonetti, M. Alexandre, J. Routaboul, C. Kerfeld, R. van Grondelle, B. Robert, J. Kennis, D. Kirilovsky, A photoactive carotenoid protein acting as light intensity sensor, Proc. Natl. Acad. Sci. U.S.A. 105 (2008) 12075–12080. https://doi.org/10.1073/pnas.0804636105.
[19] A.H. Squires, P.D. Dahlberg, H. Liu, N.C.M. Magdaong, R.E. Blankenship, W.E. Moerner, Single-molecule trapping and spectroscopy reveals photophysical heterogeneity of phycobilisomes quenched by Orange Carotenoid Protein, Nat. Commun. 10 (2019) 1172. https://doi.org/10.1038/s41467-019-09084-2.
[20] M. Gwizdala, R. Berera, D. Kirilovsky, R. van Grondelle, T.P.J. Krüger, Controlling Light Harvesting with Light, J. Am. Chem. Soc. 138 (2016) 11616–11622. https://doi.org/10.1021/jacs.6b04811.
[21] T.P.J. Krüger, R. van Grondelle, M. Gwizdala, The role of far-red spectral states in the energy regulation of phycobilisomes, Biochim. Biophys. Acta Bioenerg. 1860 (2019) 341–349. https://doi.org/10.1016/j.bbabio.2019.01.007.
[22] G. Ajlani, C. Vernotte, L. DiMagno, R. Haselkorn, Phycobilisome core mutants of Synechocystis PCC 6803, Biochim. Biophys. Acta Bioenerg. 1231 (1995) 189–196. https://doi.org/10.1016/0005-2728(95)00086-X.
[23] I. Piven, G. Ajlani, A. Sokolenko, Phycobilisome Linker Proteins Are Phosphorylated in Synechocystis sp. PCC 6803, J. Biol. Chem. 280 (2005) 21667–21672. https://doi.org/10.1074/jbc.M412967200.
[24] B. Ughy, G. Ajlani, Phycobilisome rod mutants in Synechocystis sp. strain PCC6803, Microbiology. 150 (2004) 4147–4156. https://doi.org/10.1099/mic.0.27498-0.
[25] L. Premvardhan, E. Papagiannakis, R.G. Hiller, R. van Grondelle, The Charge-Transfer Character of the S0 → S2 Transition in the Carotenoid Peridinin Is Revealed by Stark Spectroscopy, J. Phys. Chem. B. 109 (2005) 15589–15597. https://doi.org/10.1021/jp052027g.
[26] Md. Wahadoszamen, E. Belgio, Md.A. Rahman, A.M. Ara, A.V. Ruban, R. van Grondelle, Identification and characterization of multiple emissive species in aggregated minor antenna complexes, Biochim. Biophys. Acta Bioenerg. 1857 (2016) 1917–1924. https://doi.org/10.1016/j.bbabio.2016.09.010.
[27] M. Wahadoszamen, I. Margalit, A.M. Ara, R. van Grondelle, D. Noy, The role of charge-transfer states in energy transfer and dissipation within natural and artificial bacteriochlorophyll proteins, Nat. Commun. 5 (2014) 5287. https://doi.org/10.1038/ncomms6287.
[28] A.M. Ara, Md. Shakil Bin Kashem, R. van Grondelle, Md. Wahadoszamen, Stark fluorescence spectroscopy on peridinin–chlorophyll–protein complex of dinoflagellate, Amphidinium carterae, Photosynth. Res. (2019). https://doi.org/10.1007/s11120-019-00688-9.

[29] M. Wahadoszamen, R. Berera, A.M. Ara, E. Romero, R. van Grondelle, Identification of two emitting sites in the dissipative state of the major light harvesting antenna, Phys. Chem. Chem. Phys. 14 (2011) 759–766. https://doi.org/10.1039/C1CP23059J.
[30] J.M. Gruber, P. Malý, T.P.J. Krüger, R. van Grondelle, From isolated light-harvesting complexes to the thylakoid membrane: a single-molecule perspective, Nanophotonics. 7 (2018) 81–92. https://doi.org/10.1515/nanoph-2017-0014.
[31] T.P.J. Krüger, V.I. Novoderezhkin, C. Ilioaia, R. van Grondelle, Fluorescence Spectral Dynamics of Single LHCII Trimers, Biophys. J. 98 (2010) 3093–3101. https://doi.org/10.1016/j.bpj.2010.03.028.
[32] Md. Wahadoszamen, T. Hamada, T. Iimori, T. Nakabayashi, N. Ohta, External Electric Field Effects on Absorption, Fluorescence, and Phosphorescence Spectra of Diphenylpolyynes in a Polymer Film, J. Phys. Chem. A. 111 (2007) 9544–9552. https://doi.org/10.1021/jp073812r.
[33] Md. Wahadoszamen, T. Nakabayashi, S. Kang, H. Imahori, N. Ohta, External Electric Field Effects on Absorption and Fluorescence Spectra of a Fullerene Derivative and Its Mixture with Zinc-Tetraphenylporphyrin Doped in a PMMA Film, J. Phys. Chem. B. 110 (2006) 20354–20361. https://doi.org/10.1021/jp0635967.
[34] A. Moscatelli, K. Livingston, W.Y. So, S.J. Lee, U. Scherf, J. Wildeman, L.A. Peteanu, Electric-Field-Induced Fluorescence Quenching in Polyfluorene, Ladder-Type Polymers, and MEH-PPV: Evidence for Field Effects on Internal Conversion Rates in the Low Concentration Limit, J. Phys. Chem. B. 114 (2010) 14430–14439. https://doi.org/10.1021/jp101307p.
[35] G.U. Bublitz, S.G. Boxer, STARK SPECTROSCOPY: Applications in Chemistry, Biology, and Materials Science, Annu. Rev. Phys. Chem. 48 (1997) 213–242. https://doi.org/10.1146/annurev.physchem.48.1.213.
[36] T. Nakabayashi, Md. Wahadoszamen, N. Ohta, External Electric Field Effects on State Energy and Photoexcitation Dynamics of Diphenylpolyenes, J. Am. Chem. Soc. 127 (2005) 7041–7052. https://doi.org/10.1021/ja0401444.
[37] D.M. Niedzwiedzki, H. Liu, R.E. Blankenship, Excitation Energy Transfer in Intact CpcL-Phycobilisomes from Synechocystis sp. PCC 6803, J. Phys. Chem. B. 123 (2019) 4695–4704. https://doi.org/10.1021/acs.jpcb.9b02696.
[38] J.R. Reimers, M. Biczysko, D. Bruce, D.F. Coker, T.J. Frankcombe, H. Hashimoto, J. Hauer, R. Jankowiak, T. Kramer, J. Linnanto, F. Mamedov, F. Müh, M. Rätsep, T. Renger, S. Styring, J. Wan, Z. Wang, Z.-Y. Wang-Otomo, Y.-X. Weng, C. Yang, J.-P. Zhang, A. Freiberg, E. Krausz, Challenges facing an understanding of the nature of low-energy excited states in photosynthesis, Biochim. Biophys. Acta Bioenerg. 1857 (2016) 1627–1640. https://doi.org/10.1016/j.bbabio.2016.06.010.
[39] T. Renger, Theory of Optical Spectra Involving Charge Transfer States: Dynamic Localization Predicts a Temperature Dependent Optical Band Shift, Phys. Rev. Lett. 93 (2004) 188101. https://doi.org/10.1103/PhysRevLett.93.188101.
[40] S. Vaitekonis, G. Trinkunas, L. Valkunas, Red Chlorophylls in the Exciton Model of Photosystem I, Photosynth. Res. 86 (2005) 185–201. https://doi.org/10.1007/s11120-005-2747-x.
[41] T. Mančal, L. Valkunas, G.R. Fleming, Theory of exciton–charge transfer state coupled systems, Chem. Phys. Lett. 432 (2006) 301–305. https://doi.org/10.1016/j.cplett.2006.10.055.

[42] E.J.P. Lathrop, R.A. Friesner, Simulation of optical spectra from the reaction center of Rb. sphaeroides. Effects of an internal charge-separated state of the special pair, J. Phys. Chem. 98 (1994) 3056–3066. https://doi.org/10.1021/j100062a051.
[43] V. I. Novoderezhkin, R. Croce, M. Wahadoszamen, I. Polukhina, E. Romero, R. van Grondelle, Mixing of exciton and charge-transfer states in light-harvesting complex Lhca4, Phys. Chem. Chem. Phys. 18 (2016) 19368–19377. https://doi.org/10.1039/C6CP02225A.
[44] T.P.J. Krüger, V.I. Novoderezhkin, E. Romero, R. van Grondelle, Photosynthetic Energy Transfer and Charge Separation in Higher Plants, in: J. Golbeck, A. van der Est (Eds.), Biophys. Photosynth., Springer New York, New York, NY, 2014: pp. 79–118. https://doi.org/10.1007/978-1-4939-1148-6_3.
[45] D. Abramavicius, S. Mukamel, Energy-transfer and charge-separation pathways in the reaction center of photosystem II revealed by coherent two-dimensional optical spectroscopy, J. Chem. Phys. 133 (2010) 184501. https://doi.org/10.1063/1.3493580.
[46] V.M. Agranovich, Yu.N. Gartstein, A. Zakhidov, P. Bussimer, An adiabatic local model for the internal structure of charge-transfer excitons: Dimers and trimers, Chem. Phys. Lett. 110 (1984) 270–274. https://doi.org/10.1016/0009-2614(84)85227-6.
[47] V.I. Novoderezhkin, J.P. Dekker, R. van Grondelle, Mixing of Exciton and Charge-Transfer States in Photosystem II Reaction Centers: Modeling of Stark Spectra with Modified Redfield Theory, Biophys. J. 93 (2007) 1293–1311. https://doi.org/10.1529/biophysj.106.096867.
[48] L. Ying, X.S. Xie, Fluorescence Spectroscopy, Exciton Dynamics, and Photochemistry of Single Allophycocyanin Trimers, J. Phys. Chem. B. 102 (1998) 10399–10409. https://doi.org/10.1021/jp983227d.
[49] D. Loos, M. Cotlet, F. De Schryver, S. Habuchi, J. Hofkens, Single-Molecule Spectroscopy Selectively Probes Donor and Acceptor Chromophores in the Phycobiliprotein Allophycocyanin, Biophys. J. 87 (2004) 2598–2608. https://doi.org/10.1529/biophysj.104.046219.
[50] Z. Su-Ping, P. Jing-Xi, H. Zhen-Hui, Z. Jing-Quan, Y. Si-De, J. Li-Jin, Generation and identification of the transient intermediates of allophycocyanin by laser photolytic and pulse radiolytic techniques, Int. J. Radiat. Biol. (2009). https://doi.org/10.1080/095530000110039725.
[51] Q. Wang, W.E. Moerner, Dissecting pigment architecture of individual photosynthetic antenna complexes in solution, Proc. Natl. Acad. Sci. U.S.A. (2015) 201514027. https://doi.org/10.1073/pnas.1514027112.
[52] K.-H. Zhao, H. Scheer, Type I and type II reversible photochemistry of phycoerythrocyanin α-subunit from Mastigocladus laminosus both involve Z, E isomerization of phycoviolobilin chromophore and are controlled by sulfhydryls in apoprotein, Biochim. Biophys. Acta Bioenerg. 1228 (1995) 244–253. https://doi.org/10.1016/0005-2728(94)00180-D.
[53] W. Köhler, J. Friedrich, R. Fischer, H. Scheer, Site-selective spectroscopy and level ordering in C-phycocyanine, Chem. Phys. Lett. 143 (1988) 169–173. https://doi.org/10.1016/0009-2614(88)87032-5.
[54] M. Corbella, Z.S.D. Toa, G.D. Scholes, F.J. Luque, C. Curutchet, Determination of the protonation preferences of bilin pigments in cryptophyte antenna complexes, Phys. Chem. Chem. Phys. 20 (2018) 21404–21416. https://doi.org/10.1039/C8CP02541J.

[55] M.A. Mroginski, F. Mark, W. Thiel, P. Hildebrandt, Quantum Mechanics/Molecular Mechanics Calculation of the Raman Spectra of the Phycocyanobilin Chromophore in α-C-Phycocyanin, Biophys. J. 93 (2007) 1885–1894. https://doi.org/10.1529/biophysj.107.108878.
[56] H. Kikuchi, T. Sugimoto, M. Mimuro, An electronic state of the chromophore, phycocyanobilin, and its interaction with the protein moiety in C-phycocyanin: protonation of the chromophore, Chem. Phys. Lett. 274 (1997) 460–465. https://doi.org/10.1016/S0009-2614(97)00659-3.
[57] B. Zienicke, L.-Y. Chen, H. Khawn, M.A.S. Hammam, H. Kinoshita, J. Reichert, A.S. Ulrich, K. Inomata, T. Lamparter, Fluorescence of Phytochrome Adducts with Synthetic Locked Chromophores, J. Biol. Chem. 286 (2011) 1103–1113. https://doi.org/10.1074/jbc.M110.155143.
[58] G. Shen, H.S. Leonard, W.M. Schluchter, D.A. Bryant, CpcM Posttranslationally Methylates Asparagine-71/72 of Phycobiliprotein Beta Subunits in Synechococcus sp. Strain PCC 7002 and Synechocystis sp. Strain PCC 6803, J. Bacteriol. 190 (2008) 4808–4817. https://doi.org/10.1128/JB.00436-08.
[59] N. Blot, X.J. Wu, J.C. Thomas, J. Zhang, L. Garczarek, S. Böhm, J.M. Tu, M. Zhou, M. Plöscher, L. Eichacker, F. Partensky, H. Scheer, K.H. Zhao, Phycourobilin in trichromatic phycocyanin from oceanic cyanobacteria is formed post-translationally by a phycoerythrobilin lyase-isomerase., J. Biol. Chem. 284 (2009) 9290–9298. https://doi.org/10.1074/jbc.M809784200.
[60] M. Bischoff, G. Hermann, S. Rentsch, D. Strehlow, S. Winter, H. Chosrowjan, Excited-State Processes in Phycocyanobilin Studied by Femtosecond Spectroscopy, J. Phys. Chem. B. 104 (2000) 1810–1816. https://doi.org/10.1021/jp992083f.
[61] R. MacColl, Allophycocyanin and energy transfer, Biochim. Biophys. Acta Bioenerg. 1657 (2004) 73–81. https://doi.org/10.1016/j.bbabio.2004.04.005.
[62] E. Romero, M. Mozzo, I.H.M. van Stokkum, J.P. Dekker, R. van Grondelle, R. Croce, The origin of the low-energy form of photosystem I light-harvesting complex Lhca4: mixing of the lowest exciton with a charge-transfer state, Biophys. J. 96 (2009) L35-37. https://doi.org/10.1016/j.bpj.2008.11.043.
[63] S. Long, M. Zhou, K. Tang, X.-L. Zeng, Y. Niu, Q. Guo, K.-H. Zhao, A. Xia, Single-molecule spectroscopy and femtosecond transient absorption studies on the excitation energy transfer process in ApcE(1–240) dimers, Phys. Chem. Chem. Phys. 17 (2015) 13387–13396. https://doi.org/10.1039/C5CP01687H.
[64] D.J. Lundell, A.N. Glazer, Molecular architecture of a light-harvesting antenna. Core substructure in Synechococcus 6301 phycobilisomes: two new allophycocyanin and allophycocyanin B complexes., J. Biol. Chem. 258 (1983) 902–908.
[65] K. Tang, W.-L. Ding, A. Höppner, C. Zhao, L. Zhang, Y. Hontani, J.T.M. Kennis, W. Gärtner, H. Scheer, M. Zhou, K.-H. Zhao, The terminal phycobilisome emitter, LCM: A light-harvesting pigment with a phytochrome chromophore, Proc. Natl. Acad. Sci. U.S.A. 112 (2015) 15880–15885. https://doi.org/10.1073/pnas.1519177113.
[66] L. Valkunas, J. Chmeliov, T.P.J. Krüger, C. Ilioaia, R. van Grondelle, How Photosynthetic Proteins Switch, J. Phys. Chem. Lett. 3 (2012) 2779–2784. https://doi.org/10.1021/jz300983r.

[67] M. Gwizdala, J.L. Botha, A. Wilson, D. Kirilovsky, R. van Grondelle, T.P.J. Krüger, Switching an Individual Phycobilisome Off and On, J. Phys. Chem. Lett. 9 (2018) 2426–2432. https://doi.org/10.1021/acs.jpclett.8b00767.
[68] M.E. Auldridge, K.A. Satyshur, D.M. Anstrom, K.T. Forest, Structure-guided Engineering Enhances a Phytochrome-based Infrared Fluorescent Protein, J. Biol. Chem. 287 (2012) 7000–7009. https://doi.org/10.1074/jbc.M111.295121.
[69] A.J. Fischer, J.C. Lagarias, Harnessing phytochrome's glowing potential, Proc. Natl. Acad. Sci. U.S.A. 101 (2004) 17334–17339. https://doi.org/10.1073/pnas.0407645101.
[70] J. Zhang, X.-J. Wu, Z.-B. Wang, Y. Chen, X. Wang, M. Zhou, H. Scheer, K.-H. Zhao, Fused-Gene Approach to Photoswitchable and Fluorescent Biliproteins, Angew. Chem. Int. Ed. 49 (2010) 5456–5458. https://doi.org/10.1002/anie.201001094.
[71] X. Shu, A. Royant, M.Z. Lin, T.A. Aguilera, V. Lev-Ram, P.A. Steinbach, R.Y. Tsien, Mammalian Expression of Infrared Fluorescent Proteins Engineered from a Bacterial Phytochrome, Science. 324 (2009) 804–807. https://doi.org/10.1126/science.1168683.
[72] L.M.P. Beekman, R.N. Frese, G.J.S. Fowler, R. Picorel, R.J. Cogdell, I.H.M. van Stokkum, C.N. Hunter, R. van Grondelle, Characterization of the Light-Harvesting Antennas of Photosynthetic Purple Bacteria by Stark Spectroscopy. 2. LH2 Complexes: Influence of the Protein Environment, J. Phys. Chem. B. 101 (1997) 7293–7301. https://doi.org/10.1021/jp963447w.

Supplementary Information:

Stark spectroscopy

Assessing spectral heterogeneity using conventional bulk spectroscopy is difficult or impossible, since the subtle differences in the conformation of the emissive pigments and the surrounding local protein environment are generally associated with very similar transition moments, thus giving rise to identical or strongly overlapping spectral signatures. However, since the local protein environment can noticeably change the electro-optical properties and excited-state dynamics of a pigment or group of pigments, different spectral species may exhibit very different responses to an external electric field, motivating the usefulness of *SF* spectroscopy.

SF spectroscopy provides quantitative information about the molecular parameters that are connected with different physical origins, viz. changes in the molecular polarizability ($\Delta\alpha$) and dipole moment ($\Delta\mu$) between the ground and excited states, as well as the zeroth derivative contribution (ZDC). In simple terms, $\Delta\alpha$ and $\Delta\mu$ can be interpreted as, respectively, the degree of charge delocalization and charge transfer occurring in a photoactive pigment (or complex) when it undergoes an optical transition [35]. The term $\Delta\mu$ gives a direct estimate of the CT strength, while the magnitude of $\Delta\alpha$ sometimes also reflects the magnitude of the CT character [72].

SF spectroscopy mainly deals with the perturbation of the energy levels of a molecule or a molecular ensemble by a strong externally applied electric field. Several consequences can be expected in such a study.

First, a shifted *F* spectrum can be obtained due to the field-induced shift of the energy levels of the photoactive molecules. If this effect is the only contribution, the *SF* lineshape, which is commonly considered as the difference between the *F* spectra measured with and without (zero)

the electric field, would then resemble the first derivative of the (zero field) *F* spectrum, reflecting a change in $\Delta\alpha$ between the states connected by the *F* transition.

Second, a broadened *F* spectrum can be obtained due to the field-induced splitting of the energy levels. In this case, the *SF* lineshape would be similar to the second derivative of the (zero field) *F* spectrum. This appears due to a change in $\Delta\mu$ between the states associated with the *F* transition.

Third, the spectral intensity can either be decreased or increased by the presence of the electric field. In both cases, the *SF* lineshape would merely resemble the zero field *F* spectrum. Intensity changes, described by the ZDC coefficient, are believed to result from the field-induced alteration (increase or decrease) of the rates of nonradiative processes competing with *F*, provided that the field-induced change in oscillator strength or transition dipole moment is negligible. Therefore, an *SF* spectrum can essentially be considered as a resultant sum of the three above-mentioned field-induced effects.

Supplementary Figures

Figure S1

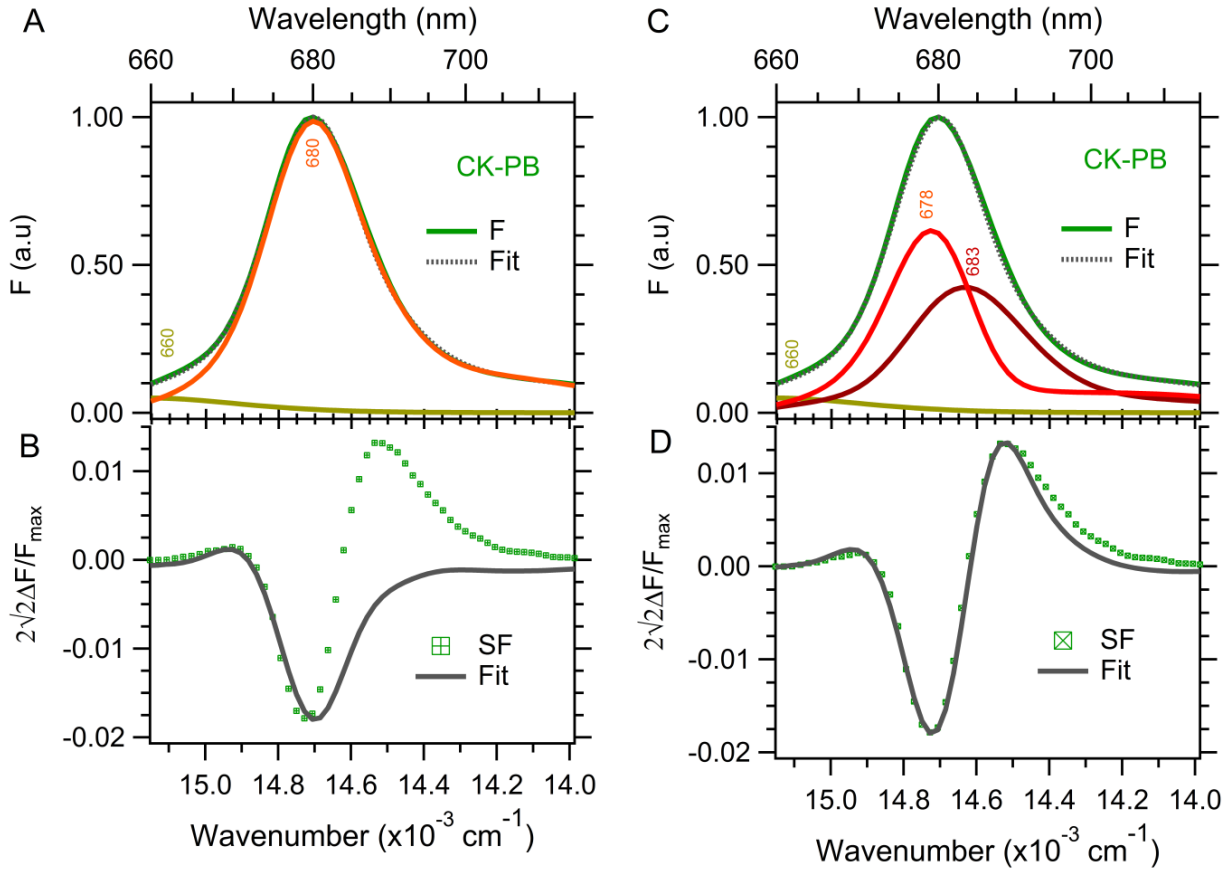

Fig. S1 Modeling of the *SF* spectrum (B and D) of CK-PB upon deconvoluting the corresponding *F* spectrum into (A) two bands, peaking at 660 and 680 nm, and (C) three bands, peaking at 660 nm, 678 nm and 683 nm). In (C) and (D), the spectral deconvolution of the *F* intensity above 690 nm includes vibrational progression of the 678 nm and 683 nm bands.

Figure S2

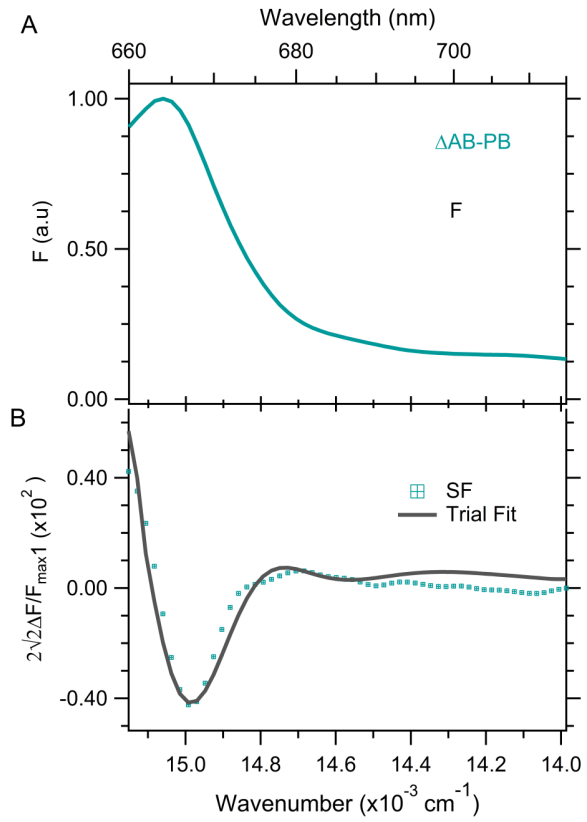

Fig. S2 Modeling of the *SF* spectrum (B) of ΔAB-PB with the *F* spectrum (A), including only vibrational progression.

Figure S3

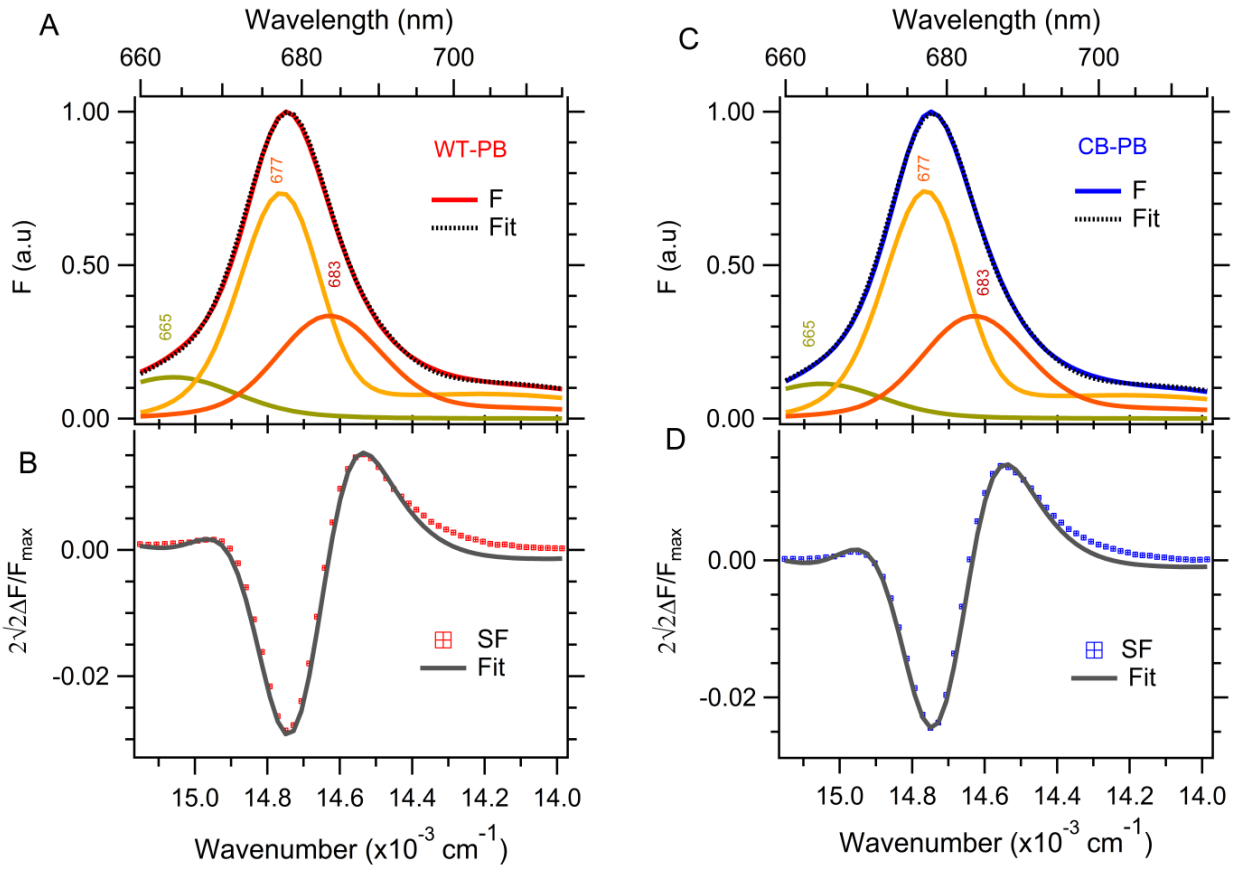

Fig. S3 Modeling of the *SF* spectrum of WT-PB (B) and CB-PB (D) upon deconvoluting the corresponding *F* spectra (A and C) into three bands (peaking at 665 nm, 678 nm and 683 nm). The spectral deconvolution in (A and C) was implemented by assuming that the *F* intensity above 690 nm constitutes only the vibrational progression of the 677 nm and 683 nm bands.

Figure S4

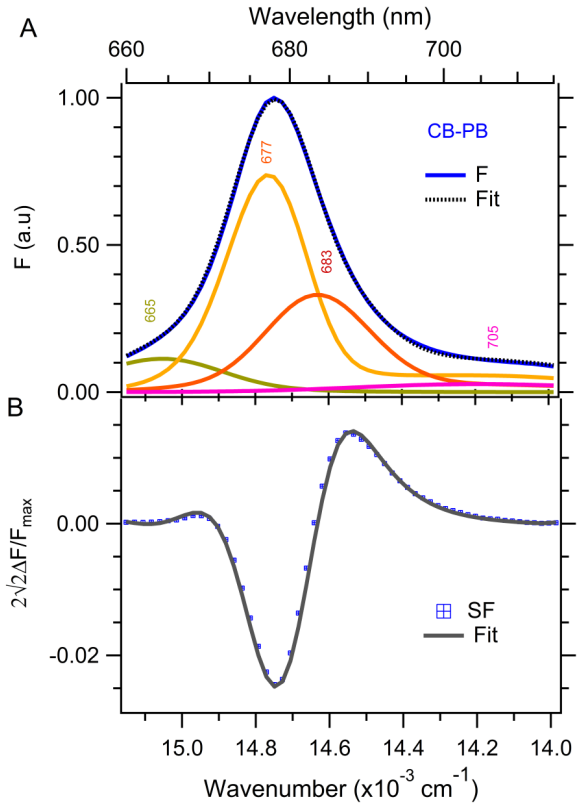

Fig. S4 Modeling of the *F* (A) and *SF* (B) spectra of CB-PB performed in an identical way as for WT-PB in Fig. 1H and I.

Figure S5

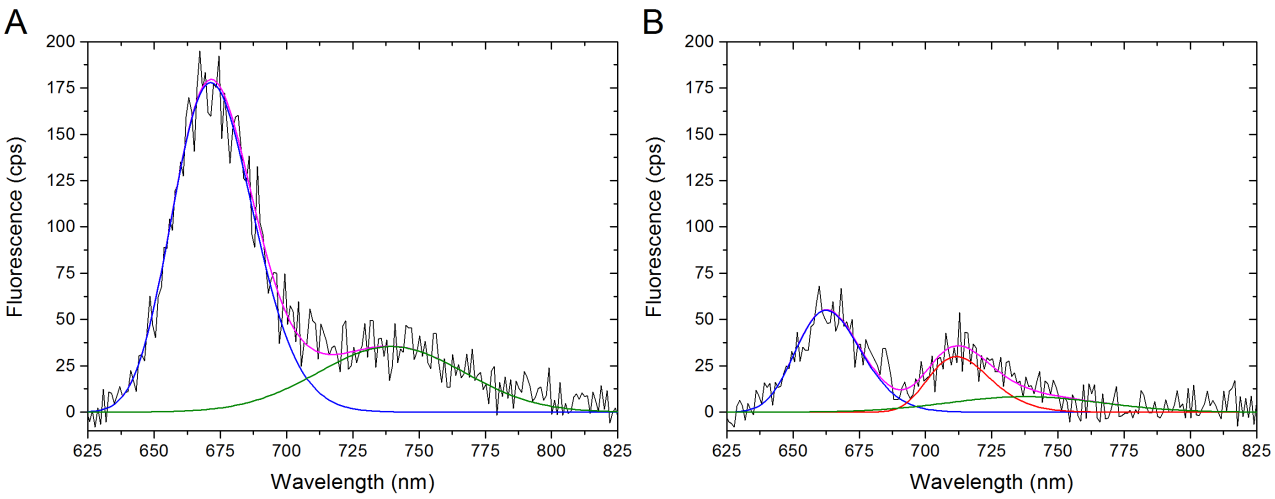

Fig. S5 Single-molecule spectrum resembling an unquenched state, peaking at ~670 nm (A), and a spectrum resembling a far-red emission state, characterized by two distinct bands peaking at ~663 nm and 712 nm, respectively, and a reduced intensity (B). Both spectra are from the same WT-PB complex and were measured for 1 s each after excitation of 1.8 W/cm^2. Data is shown in black, the fit of the 660-670-nm band is blue, the fit of the far-red component is red, and the fit of the vibrational band is green. For the fit of the vibrational band in B, the average fitting parameters of all other vibrational bands in the spectral sequence were used; only the amplitude was scaled to that of the main, 660-670-nm band.